RESEARCH ARTICLE
doi: 10.2306/scienceasia1513-1874.2025.085

ScienceAsia 51 (5): 2025: ID 2025085: **1–11**

Absorption and emission spectral response triggered by dipicolinate in a composite structure of luminescent metal framework and rose bengal dye

Xinhua Qin[a], **Mimi Wang**[b,*], **Yangyang Ou**[c], **Fei Wang**[d,*]

[a] Department of Mechanical and Electrical Engineering, Lvliang Vocational and Technical College, Lvliang 032300 China
[b] College of Design and Architecture, Zhejiang Wanli University, Ningbo, Zhejiang 315100 China
[c] Guizhou University, Guiyang, Guizhou 550025 China
[d] School of Material SCI. & Eng., Zhengzhou University, Zhengzhou 450001 China

*Corresponding authors, e-mail: mmwang@ahjzu.edu.cn, wryh80@126.com

Received 7 Mar 2024, Accepted 28 Aug 2025
Available online 31 Oct 2025

ABSTRACT: Calcium dipicolinate (CaDPA) is a biomarker for *Bacillus anthracis* spores. This study introduced a novel structure designed for the optical sensing of DPA. It used a luminescent metal-organic framework (MOF) doped with Eu ions as the supporting lattice and an organic dye derived from rose bengal as the sensing probe. The composite structure was fully characterized, including XRD, IR, TGA, and photophysical analyses. Detailed analysis confirmed the dual sensing capabilities of this structure, which were the colorimetric sensing reliant on absorption and ratiometric fluorescent sensing reliant on fluorescence. Linear sensing response was detected, with a limit of detection value of 2.2 μM. The sensing mechanism was revealed as a combination of the emission turn-on effect of the rose bengal probe and the emission turn-off effect of the Eu-based supporting lattice. This composite structure demonstrated superiority over conventional MOF sensing materials due to its dual sensing abilities and potential for naked-eye detection.

KEYWORDS: MOF composite, biomarker, emission turn on-off, emission lifetime

INTRODUCTION

Endothermic creatures, including humans, can be infected by anthrax, a well-known acute ailment, when exposed to *Bacillus anthracis* spore concentrations exceeding 10^4 [1, 2]. Because of their remarkable ability to survive in harsh environments, *B. anthracis* spores are sometimes utilized as a biological weapon. The imperative for public safety in medical services and counter-terrorism necessitates fast and dependable detection methods for this biological hazard. Among the various studies conducted on *B. anthracis* spores, calcium dipicolinate (CaDPA) has emerged as a distinctive component, rendering it a unique biomarker for *B. anthracis* spores [3]. The concentration of CaDPA can be easily determined with various analytical techniques, such as chemical and biological assays [4]. Despite the precision afforded by these methods, their unsuitability for rapid and real-time detection is evident due to the inherent drawbacks including time-consuming procedures, sample preparation requirements, complex instrumentation, and high costs [5, 6].

Sensing detection is a viable method for identifying the biomarkers due to its rapid response, minimal instrumentation requirements, low costs, and straightforward sample preparation procedures [7]. For example, Niyomdecha et al reported an in-house photoactivator modified by azo dye to improve the detection of human (OC43) coronavirus surrogate and SARS-CoV-2 viability [8]. During these efforts, various nano-platforms have been investigated. For example, Long et al developed a Ru-Co bimetallic sepiolite for photoreaction and photocatalysis [9]. Cao et al improved the non-enzymatic glucose sensing performance with ZnO@ZIF-67 nanoarrays [10]. Shu et al improved the optical properties of amorphous films doped with germanium quantum dots [11]. In most reported optical sensing systems for DPA, the intensity of their emission (or lifetimes) decreases as the DPA concentration increases [7, 12]. Essentially, these systems operate on an emission turn-off principle. However, due to the possibility of emission quenching by environmental factors and other emission quenchers, these emission-turn-off sensing structures often exhibit poor selectivity and limited accuracy. It is hypothesized that employing emission-turn-on probes could solve this issue. Nevertheless, achieving this with conventional luminescent probes is challenging, as DPA's electron-attracting properties effectively act as emission quenchers. Consequently, novel sensing structures with an emission turn-on effect for DPA detection should be devised.

Recently, a versatile structure of metal-organic frameworks (MOFs) for various applications such as gas separation, drug adsorption/desorption, and catalysis has been established [13]. Some of these frameworks even exhibit luminescence and are being developed for optical sensing [14]. For instance, Zhang et al have reported an optical sensing material by co-doping Eu(III) and Tb(III) ions into luminescent MOFs [15].

Additionally, organic dyes are incorporated into these MOFs to achieve integrated or enhanced performance. For example, composite samples of dye-MOFs typically exhibit multiple emission bands. When only one of these bands is sensitive to the analyte, while the others remain constant and serve as internal references, self-calibrated signals can be obtained, demonstrating ratiometric optical sensing and enhancing precision and selectivity [16, 17].

Considering the aforementioned factors, a composite structure for DPA optical sensing (labeled as RPh@EuBTC) was designed, comprising two working components: a sensing agent derived from rose bengal 6G (RPh) and a luminescent MOF based on rare earth (EuBTC). In the subsequent sections, a detailed account of this composite structure and its sensing capabilities is presented.

MATERIALS AND METHODS

General information

The synthetic route of RPh@EuBTC is shown in Scheme 1. All initial compounds were of AG grade quality and supplied by Aldrich Chemical Corporation (Shanghai, China), including 1,3,5-benzenetricarboxylic acid (H_3BTC), $Eu(NO_3)_3$, rose bengal 6G, hydrazine (95%), 4-hydroxybenzaldehyde, 1-ethyl-3-(3-dimethylaminopropyl) carbodiimide hydrochloride (EDC), and N-hydroxysuccinimide (NHS). The characterization of samples, including NMR, MS, IR, and XRD analyses, was conducted utilizing a Varian (Palo Alto, USA) INOVA 300 spectrometer, an Agilent (Santa Clara, USA) 1100 MS spectrometer, a Bruker (Billerica, USA) Vertex 70 FTIR spectrometer (KBr pellet technique), and a Rigaku (Tokyo, Japan) X-ray diffractometer (with a wavelength of 1.5418 Å), respectively. Sample morphology was examined using a Hitachi (Tokyo, Japan) S-4800 microscope. Photophysical measurements were carried out using an Agilent 8453 UV-Vis-NIR diode array spectrophotometer and a Hitachi F-7000 fluorescence spectrophotometer. Emission lifetimes were determined utilizing a Lecroy (New York, USA) Wave Runner 6100 Digital Oscilloscope (1 GHz) excited by a tunable laser source (Continuum Sunlite OPO, Boston, USA) and a FL980 (Edinburgh, Livingston, Scotland) fluorescence lifetime spectrometer excited by a hydrogen flash lamp.

Synthesis of sensing probe precursor RPh

Initially, R6-NH2 was synthesized following a literature protocol using rose bengal 6G and hydrazine as starting materials [18]. A solution of rose bengal 6G (2 g), anhydrous hydrazine (5 ml), and ethanol (20 ml) was stirred at 80 °C for 12 h under a nitrogen atmosphere. Following the removal of solvent and excess hydrazine under reduced pressure, a crude product was obtained and subsequently purified by recrystallization in ethanol/water (V/V = 4:6). ^{1}HNMR ($CDCl_3$), δ (ppm): 8.11–8.02 (m, 1H), 7.58 (m, 1H), 7.42–7.30 (m, 2H), 6.97 (s, 2H), 6.12 (s, 2H), 4.66 (NH), 4.41 (NH), 3.20 (m, 4H), 2.29 (s, 6H), 1.28 (t, J = 6.1 Hz, 6H). ^{13}C NMR (DMSO-d_6, 75 MHz), δ (ppm): 165.40, 150.54, 147.73, 142.10, 132.56, 129.33, 128.47, 127.29, 126.46, 123.25, 123.07, 112.69, 99.86, 63.86, 39.13, 17.86, 14.44. MS m/z: $[m]^+$ calc. for $C_{26}H_{28}N_4O_2$, 428.2; found, 428.4.

The R6-NH_2 obtained above (2 mmol) was combined with 4-hydroxybenzaldehyde (3 mmol) and ethanol (30 ml) [18]. This mixture was heated at 80 °C for 12 h under a nitrogen atmosphere. Upon evaporation of the solvent under reduced pressure, the resulting solid residue was purified using a silica gel column with CH_2Cl_2 as the eluent. ^{1}HNMR ($CDCl_3$), δ (ppm): 8.10–8.01 (m, 1H), 7.62–7.51 (m, 4H), 7.42–7.30 (m, 3H), 6.96 (s, 2H), 6.93–6.83 (m, 2H), 6.12 (s, 2H), 4.66 (t, J = 3.8 Hz, 2H), 3.20 (m, 4H), 2.28 (s, 6H), 1.28 (t, J = 6.1 Hz, 6H). ^{13}C NMR (DMSO-d_6, 75 MHz), δ (ppm): 163.02, 155.33, 149.41, 147.98, 145.77, 144.13, 132.66, 131.03, 129.74, 128.64, 127.95, 127.13, 126.19, 123.80, 123.21, 114.30, 114.13, 100.05, 56.55, 39.13, 17.80, 13.88. ESI-MS m/e: calc. for $C_{33}H_{32}N_4O_3$, 532.3; found, 532.5 $[m]^+$.

Fabrication of luminescence rare earth MOF EuBTC

The supporting framework EuBTC was synthesized following a literature procedure [19]. Initially, a solution of $Eu(NO_3)_3$ (1.0 mmol) and NaAc (3.0 mmol) in deionized water (30 ml) was prepared and ultrasonicated for 20 min. Another solution of H_3BTC dissolved in ethanol (1.0 mmol in 30 ml) was prepared and added to the previous solution. This mixture was stirred for 2 h at room temperature. The resulting solid was collected, washed with ethanol, and dried to yield EuBTC. Elemental analysis, C: 23.03, N: 0.09.

Synthesis of the dye-MOF composite structure RPh@EuBTC

The composite structure of dye-MOF, RPh@EuBTC, was synthesized as follows. A solution of EuBTC in ethanol (0.5 mmol in 40 ml) was combined with EDC (1.0 mmol) and NHS (1.0 mmol). After stirring at room temperature for 30 min, this solution was slowly added dropwise to a solution of RPh in DMF (1.0 mmol in 10 ml). The resulting mixture was further stirred at room temperature for 24 h. The solid product was collected and washed with ethanol to yield RPh@EuBTC. Elemental analysis, C: 34.33, N: 1.71.

RESULTS AND DISCUSSION

Characterization of RPh@EuBTC

Micromorphology and XRD

The morphology of RPh@EuBTC and its supporting lattice, EuBTC, is conducted using their SEM images. As depicted in Fig. 1, the supporting lattice of EuBTC is smooth-surfaced nanorods with a random distribution.

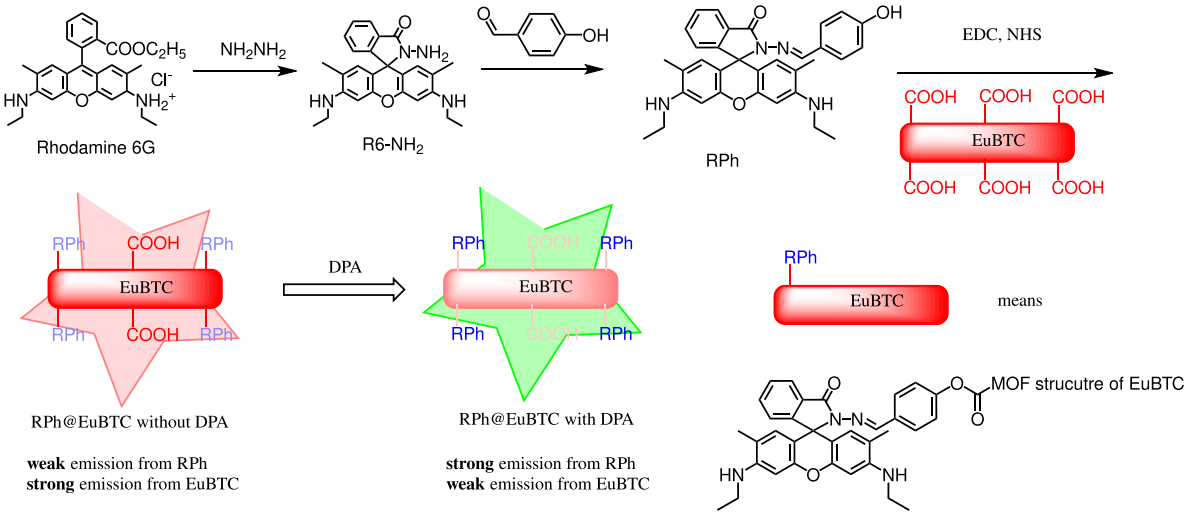

Scheme 1 Schematic representation of the preparation route for RPh@EuBTC.

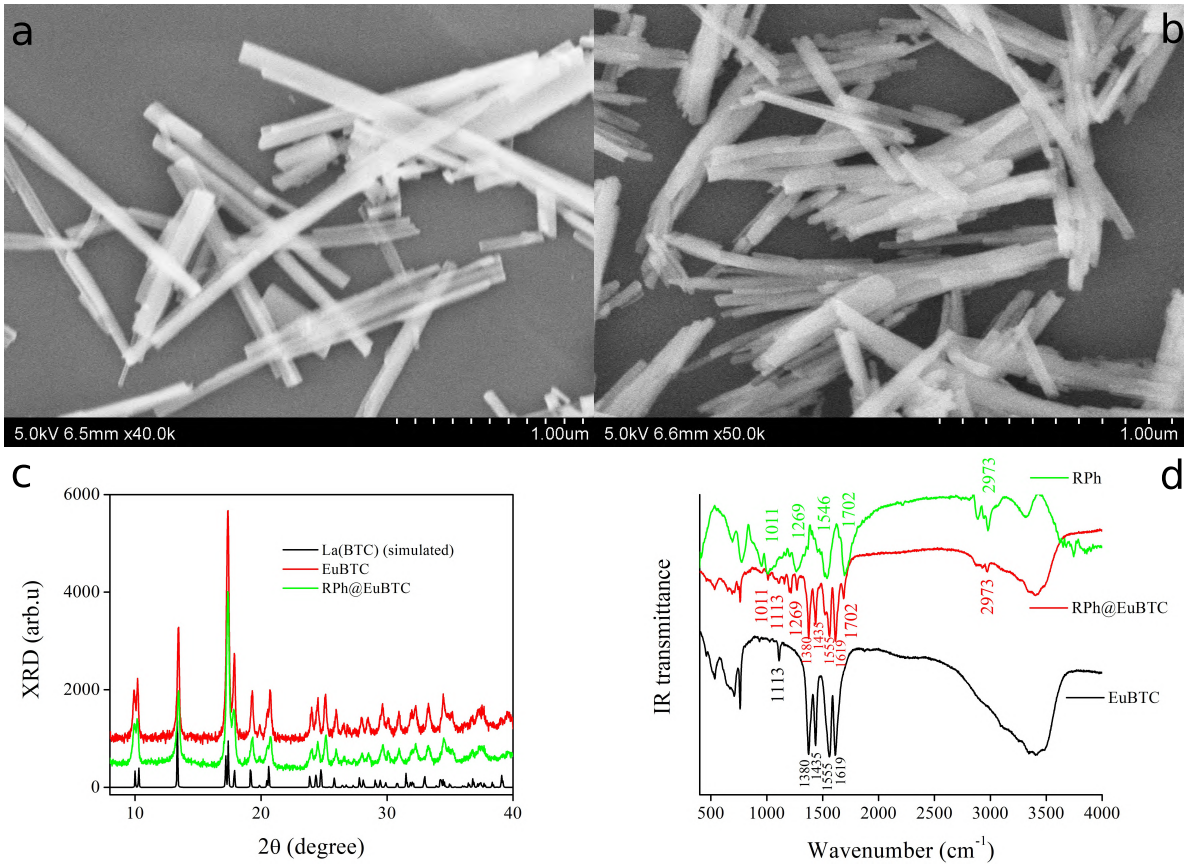

Fig. 1 SEM images of supporting lattice EuBTC (a) and RPh@EuBTC (b); XRD patterns (c) of La(BTC), RPh@EuBTC, and EuBTC; arb.u = arbitrary unit; IR spectra (d) of RPh, EuBTC, and RPh@EuBTC.

Their average width and length are determined as approximately 80 nm and 1.0 µm, respectively, which align with the values reported in literature for similar rare earth MOF samples [19]. Upon treatment with RPh, these nanorods are still distributed randomly without a distinct orientation. Some shorter nanorods, measuring around 200 nm in length, are observed, yet their morphology and width resemble those of the

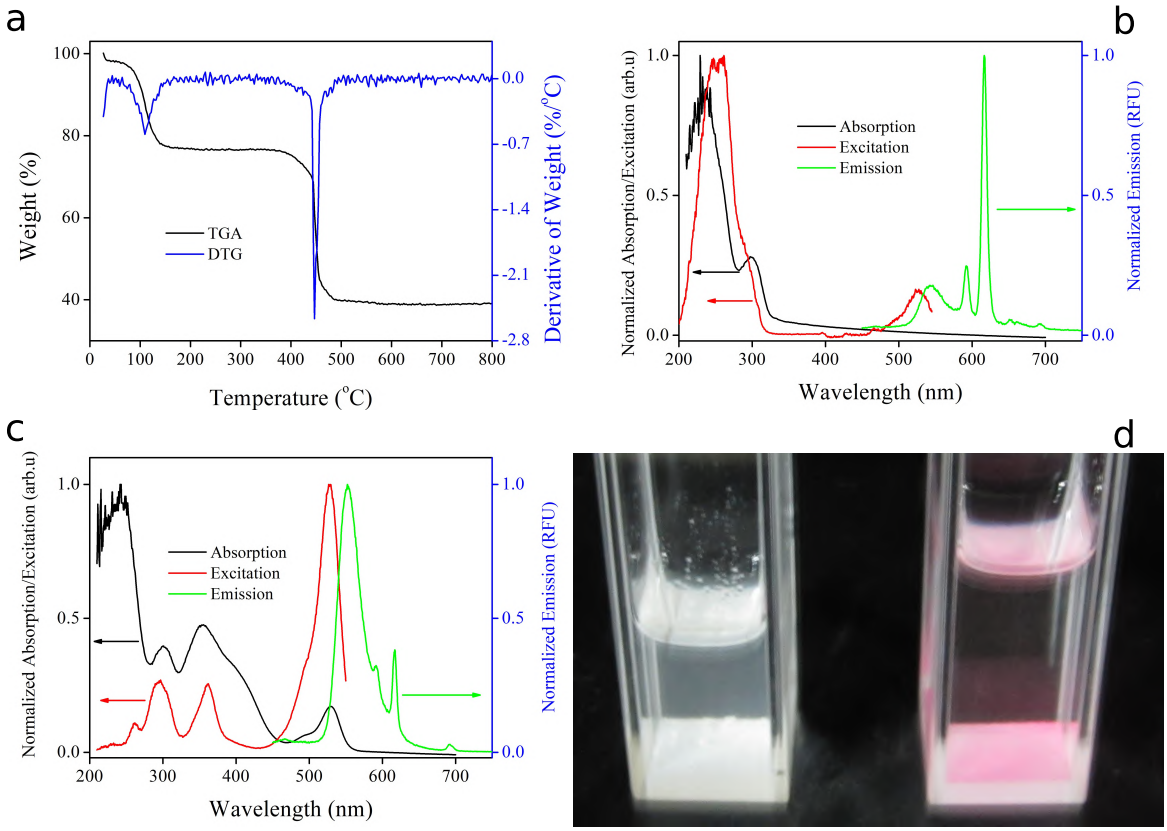

Fig. 2 TGA and DTG measurement (a) of RPh@EuBTC. Absorption, excitation, and emission spectra (b) of RPh@EuBTC in ethanol (0.05 mg/ml), and those (c) in the presence of DPA (100 μM); arb.u = arbitrary unit, RFU = relative fluorescence unit. Photograph (d) of RPh@EuBTC suspension in ethanol (0.05 mg/m) under daylight with DPA concentrations of 0 μM (left) and 10 μM (right).

original EuBTC nanorods. Some long EuBTC nanorods may have fractured into shorter ones; nevertheless, their crystal lattice remains intact throughout this process.

The aforementioned assumption is validated through the XRD patterns of RPh@EuBTC and EuBTC. As illustrated in Fig. 2, both samples exhibit remarkably similar XRD patterns. Within the 2θ range from 9° to 26°, ten distinct sets of characteristic peaks are observed in each sample. These diffraction peaks closely resemble those of a reference sample, La(BTC) (CCDC 290771), with minimal spectral shifting. Consequently, it is confirmed that EuBTC shares the same crystal lattice with La(BTC). Despite the treatment with the sensing probe RPh, the crystal lattice of EuBTC remains well preserved. However, this modification does affect the crystal regularity of the supporting matrix, EuBTC, resulting in a reduction in the diffraction intensity of RPh@EuBTC compared to that of EuBTC. This finding corroborates the observation of fractured nanorods depicted in Fig. 1.

IR, TGA, and elemental analysis

To gain insight into RPh@EuBTC and its probe loading status, Fig. 3 displays its IR spectrum alongside those of the supporting lattice EuBTC and the sensing probe RPh. EuBTC has a straightforward molecular structure, resulting in a simple IR spectrum with only a few characteristic bands. The initial band, peaking at 1113 cm^{-1}, corresponds to the stretching vibration of the O=C–OR bond. Two sharp IR bands at 1380 cm^{-1} and 1435 cm^{-1} represent the stretching vibration of free –COOH bonds on the surface of EuBTC. Additionally, two robust IR bands at 1555 cm^{-1} and 1619 cm^{-1} are assigned to the symmetric and asymmetric bending vibrations of the C=O bond. Concerning the sensing probe RPh, several characteristic bands are observed, with peaks at 1011 cm^{-1}, 1269 cm^{-1}, 1546 cm^{-1}, 1702 cm^{-1}, and 2973 cm^{-1}, respectively. Specifically, the IR bands at 1011 cm^{-1} and 1546 cm^{-1} correspond to the stretching and symmetric bending vibrations of the C=O bond, respectively [20]. Furthermore, the IR bands at 1269 cm^{-1} and 1702 cm^{-1} are attributed

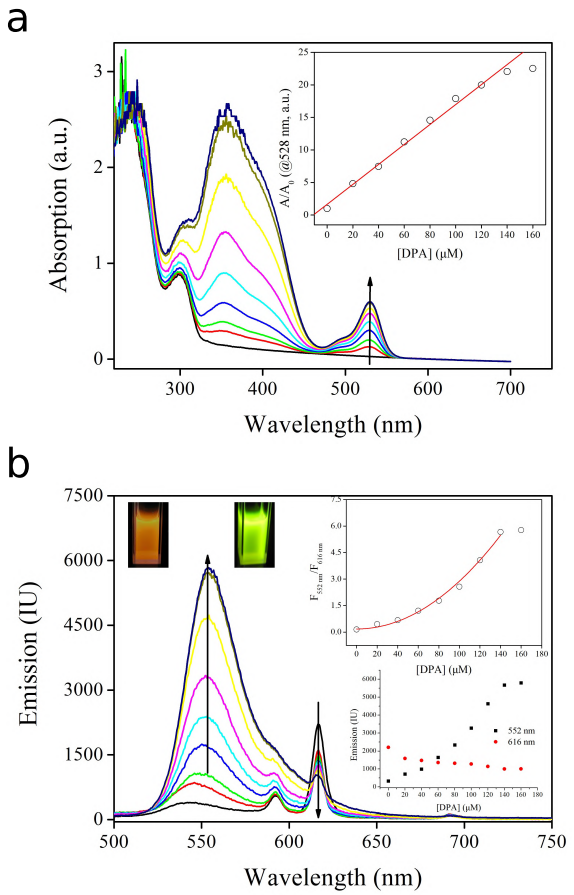

Fig. 3 Absorption (a) and emission (b) spectra of RPh@EuBTC suspension in ethanol (0.05 mg/ml) under various DPA concentrations from 0 to 160 μM (interval = 20 μM); a.u. = absorbance unit, IU = intensity unit. Inset: A/A_0, $F_{552\,nm}/F_{616\,nm}$, and emission intensity at 552 nm and 616 nm against DPA concentration, and photographs of RPh@EuBTC suspension with DPA concentrations of 0 μM (left) and 160 μM (right). Each data point represents the mean value of three test cycles.

to the stretching and symmetric bending vibrations of the C=N bond, respectively. A series of IR bands around 2973 cm^{-1} belong to the stretching vibration of the —NHEt group. The characteristic IR bands of EuBTC and RPh are all evident in the IR spectrum of RPh@EuBTC, including 1011 cm^{-1} (RPh, stretching C=O), 1113 cm^{-1} (EuBTC, stretching O=C—OR), 1269 cm^{-1} (RPh, stretching C=N), 1380 cm^{-1} (EuBTC, stretching —COOH), 1435 cm^{-1} (EuBTC, stretching —COOH), 1555 cm^{-1} (RPh/EuBTC, symmetric bending C=O), 1619 cm^{-1} (EuBTC, asymmetric bending C=O), 1702 cm^{-1} (RPh, symmetric bending C=N), and 2973 cm^{-1} (RPh, stretching —NHEt). Only minimal spectral shifts are observed for these IR bands in RPh@EuBTC compared to those in EuBTC and RPh. It is concluded that the sensing probe RPh has been covalently attached to EuBTC by forming —CO—O bonds.

To further understand the covalent bonding between the sensing probe (RPh) and the supporting lattice (EuBTC) in RPh@EuBTC, Fig. 2 presents its thermogravimetric analysis (TGA) measurement. Corresponding derivative thermogravimetry (DTG) analysis is also provided to assist weight loss assignment. Two primary weight loss regions are identified, ranging from 65 °C to 165 °C and from 403 °C to 500 °C, respectively. The first region exhibits an endothermic peak at 108 °C with a weight loss of 23.6%. This value closely matches the water content in EuBTC · 6 H_2O (23.1%). Thus, the initial weight loss region is assigned as the thermal evaporation of crystal water in the supporting lattice EuBTC. Subsequently, a further weight loss of 37.5% is observed in the second weight loss region with an endothermic temperature of 446 °C. This TGA curve maintains stability at higher temperatures. Considering the high endothermic temperature and significant weight loss, this region is attributed to the thermal collapse and degradation of the MOF lattice. Apart from these two weight loss regions, no thermal release corresponding to RPh is detected. This result confirms the covalent bonding between RPh and EuBTC.

The probe loading level in RPh@EuBTC is determined by comparing the elemental analysis results of RPh@EuBTC and EuBTC. The carbon (C) content in the as-synthesized supporting matrix EuBTC is determined as 23.03%, which closely aligns with the calculated C component of EuBTC (23.12%). The minimal nitrogen (N) content in EuBTC (0.09%) may be the residual material from the sample preparation process. Following probe loading, RPh@EuBTC exhibits increased C and N contents of 34.33% and 1.71%, respectively. Assuming that these increased C and N contents originate from the sensing probe RPh, the probe loading level in RPh@EuBTC is calculated as 15.2%. This value is consistent with literature values for similar composite structures [15]. Considering the above-mentioned covalent bonding between the probe and EuBTC, the probe loading level is limited by the amount of dangling —COOH group on EuBTC surface. To improve the probe loading level, a host with a higher surface area should be used, such as porous-structured or particle EuBTC.

Photophysical performance: Absorption, emission, and excitation

This sensing composite structure is analyzed based on its absorption, emission, and excitation spectra, as depicted in Fig. 2. The as-synthesized RPh@EuBTC exhibits strong absorption in the UV region, ranging from 210 nm to 335 nm, with two absorption bands peaking at 238 nm and 300 nm, respectively. These bands are attributed to the ligand $\pi-\pi^*$ absorption of EuBTC due to their similarity in absorption coefficients and wavelength to those of the ligand BTC [19]. In the

visible region, the absorption is relatively weak, ending at ∼440 nm, which makes RPh@EuBTC colorless under daylight conditions. No noticeable absorption from the rose bengal open-ring structure around 520 nm is detected, indicating that the probe molecules in RPh@EuBTC exist in a thermally stable spirolactam structure [18]. Only two excitation bands are identified for RPh@EuBTC, peaking at 260 nm and 524 nm, respectively. The first excitation band in the UV region closely resembles the ligand $\pi - \pi^*$ absorption and is thus designated as BTC energy transfer to the emissive Eu ions. The second excitation band in the visible region is weaker, having no obvious absorption band associated with it. It is tentatively attributed to rose bengal (xanthene structure) energy transfer to the emissive Eu ions. With excitation wavelength of 260 nm, RPh@EuBTC displays five characteristic emission bands, peaking at 545 nm, 592 nm, 616 nm, 652 nm, and 693 nm, respectively. Notably, the first emission band corresponds to rose bengal emission, while the remaining four emission bands are assigned as $^5D_0 \rightarrow {}^7F_J$ (J = 1–4) transitions of emissive Eu ions. The higher intensity of the $^5D_0 \rightarrow {}^7F_2$ emission (616 nm) compared to the $^5D_0 \rightarrow {}^7F_1$ emission suggests a low-symmetry microenvironment around these emissive Eu ions, which is consistent with the literature findings [21].

The DPA sensing performance of RPh@EuBTC is initially assessed by comparing its photophysical spectra before and after exposure to DPA. As depicted in Fig. 2, the absorption bands of RPh@EuBTC at 238 nm and 300 nm remain unchanged in the presence of DPA, with only slight spectral shifts caused by the electron-withdrawing effect of DPA. This observation suggests that DPA molecules have minimal impact on the ligand $\pi - \pi^*$ absorption. However, two new absorption bands, peaking at 355 nm and 528 nm, are observed compared to the absorption bands of free RPh@EuBTC. After cross-referencing the absorption wavelengths and coefficients of similar rose-bengal-based dyes, these two new absorption bands are attributed to the absorption of the rose bengal xanthene structure [18, 19]. Consequently, it is inferred that rose bengal molecules undergo a structural transformation from the thermally stable spirolactam structure to the emissive xanthene structure in the presence of DPA. Given that these two absorption bands fall within the visible region, an increase in their intensity is expected to induce a color change in RPh@EuBTC, thereby facilitating a colorimetric sensing response to DPA.

When DPA is introduced into the suspension of RPh@EuBTC, four excitation bands are observed, peaking at 260 nm, 297 nm, 362 nm, and 528 nm. The first two excitation bands align well with the ligand $\pi - \pi^*$ absorption and are thus assigned as ligand energy transfer to the emissive Eu ions. The following two excitation bands are tentatively attributed to the energy transfer from the rose bengal xanthene structure to the emissive Eu ions. Compared to those of free RPh@EuBTC, these two excitation bands show significant enhancement. Additionally, it is noteworthy that the ligand excitation bands (260 nm and 297 nm) are considerably weakened compared to those of free RPh@EuBTC, likely due to the formation of the rose bengal xanthene structure. Four emission bands are observed for RPh@EuBTC in the presence of DPA, peaking at 552 nm, 591 nm, 617 nm, and 693 nm, respectively. The first emission band is attributed to rose bengal emission, while the other three emission bands are attributed to Eu emission bands. The rose bengal emission band of DPA-treated RPh@EuBTC exhibits an increase in intensity and a red shift compared to that of free RPh@EuBTC. On the other hand, the Eu emission bands show a significant decrease. To systematically compare the two emission components of RPh@EuBTC, an emission intensity ratio of $F_{552\,nm}/F_{616\,nm}$ is defined. In the absence of DPA, a low $F_{552\,nm}/F_{616\,nm}$ value of 0.15 is calculated. Upon the addition of DPA, the $F_{552\,nm}/F_{616\,nm}$ value increases by 17 times to 2.57. In this case, self-calibrated sensing signals are obtained for ratiometric fluorescent sensing.

Colorimetric and ratiometric fluorescent sensing behavior of RPh@EuBTC towards DPA

As previously stated, RPh@EuBTC offers two channels for sensing DPA: colorimetric sensing and ratiometric fluorescent sensing. The following section discusses these two sensing techniques and their respective performance in detail.

Colorimetric sensing

The colorimetric sensing performance of RPh@EuBTC towards DPA is discussed based on its absorption spectra under various DPA concentrations, as depicted in Fig. 3. As the DPA concentration increased from 0 to 160 μM (with intervals of 20 μM), the ligand $\pi - \pi^*$ absorption around 238 nm remains consistent in both intensity and wavelength. However, the absorption bands of rose bengal, peaking at 355 nm and 528 nm, show significant augmentation, indicating that more rose bengal sensing molecules begin to take the fluorescent xanthene structure in the presence of DPA. Concurrently, a visible color change from colorless to red is anticipated under daylight conditions, demonstrating the colorimetric sensing behavior towards DPA. To validate this assumption, we focus on the absorption band at 528 nm in the visible region for further examination. The inset in Fig. 3a displays the absorption intensity ratio (A/A_0) versus the variation in DPA concentration, where "A" represents the absorbance value, "A_0" is the absorbance value at a DPA concentration of 0 μM, and [DPA] denotes the DPA concentration. A linear working curve is observed within the working range from 0 to 140 μM. The corresponding fitting equation is

obtained as $A/A_0 = 1.6381 + 0.1535 \times [DPA]$, with an R^2 value of 0.9962. However, upon a higher DPA concentration of 160 μM, there is no discernible increase in the absorption of RPh@EuBTC at 528 nm, indicating that RPh@EuBTC has reached its maximum sensing capacity. In accordance with a literature method ($3\sigma/N$), the limit of detection (LOD) value is calculated as 2.2 μM [18]. This low LOD value demonstrates a significant improvement compared to literature values [18–21].

Ratiometric fluorescent sensing

The ratiometric fluorescent sensing performance of RPh@EuBTC towards DPA is tentatively explored based on its emission spectra at various DPA concentrations. As depicted in Fig. 3, RPh@EuBTC exhibits five distinct emission bands in the absence of DPA, peaking at 545 nm, 592 nm, 616 nm, 652 nm, and 693 nm, respectively. Upon increasing DPA concentration from 0 to 140 μM, the rose bengal emission experiences significant enhancement, while the Eu emission bands (at 592 nm, 616 nm, 652 nm, and 693 nm) undergo considerable quenching. In fact, most of the Eu emission bands are overshadowed by the rose bengal emission at corresponding wavelengths. Notably, the rose bengal emission of RPh@EuBTC displays a slight red shift from 545 nm at a DPA concentration of 0 μM to 552 nm at a DPA concentration of 140 μM, which may be attributed to the increasing electron-withdrawing effect of DPA. Most traditional emissive MOF materials for sensing applications typically exhibit a single emission band in each sample. In contrast, RPh@EuBTC demonstrates an advantage by providing self-calibrated sensing signals, needing no auxiliary references throughout the sensing operation [22]. The emission color of RPh@EuBTC suspension turns from orange (CIE x = 0.503, y = 0.443) at DPA concentration of 0 μM to greenish yellow (CIE x = 0.410, y = 0.575) at DPA concentration of 160 μM, as shown in Fig. 3b, confirming the possibility of ratiometric sensing. In this case, the characteristic Eu emission band at 616 nm is designated as the inner reference and the rose bengal emission intensity at 552 nm as the sensing signal. The inset in Fig. 3 illustrates the emission intensity ratio ($F_{552\,nm}/F_{616\,nm}$) versus the variation in DPA concentration, where "$F_{552\,nm}$" represents the emission intensity at 552 nm, "$F_{616\,nm}$" denotes the emission intensity at 616 nm, and [DPA] stands for DPA concentration. Unlike the straight linear working curve of A/A_0 vs. [DPA], a non-linear fitting equation of $0.176 + 2.7 \times 10^{-4} \times [DPA]^2$, with an R^2 value of 0.993, was observed for $F_{552\,nm}/F_{616\,nm}$ vs. [DPA] within the DPA concentration range of 0 to 140 μM. As shown in the inset of Fig. 3, the emission intensity at 552 nm shows down-bending tendency within this region. Considering the spectral overlap between the absorption and emission of RPh@EuBTC shown in Fig. 2c, the decrease in probe emission at 552 nm is attributed to the probe self-absorption. In addition, the decreasing emission intensity at 616 nm increases the non-linearity of the working curve of $F_{552\,nm}/F_{616\,nm}$ vs. [DPA]. According to a literature method ($3\sigma/N$), the limit of detection (LOD) value is calculated as 9.9 μM [18]. This LOD value ensures a low false alarm rate at low DPA concentrations. When [DPA] exceeds a critical level (LOD value), distinct sensing signals will be generated, serving as a warning signal for DPA concentrations reaching hazardous levels. At an even higher DPA concentration of 160 μM, there is no discernible increase in the rose bengal emission at 552 nm, indicating that RPh@EuBTC has reached its maximum sensing capacity, and this observation is consistent with the observation in its colorimetric sensing.

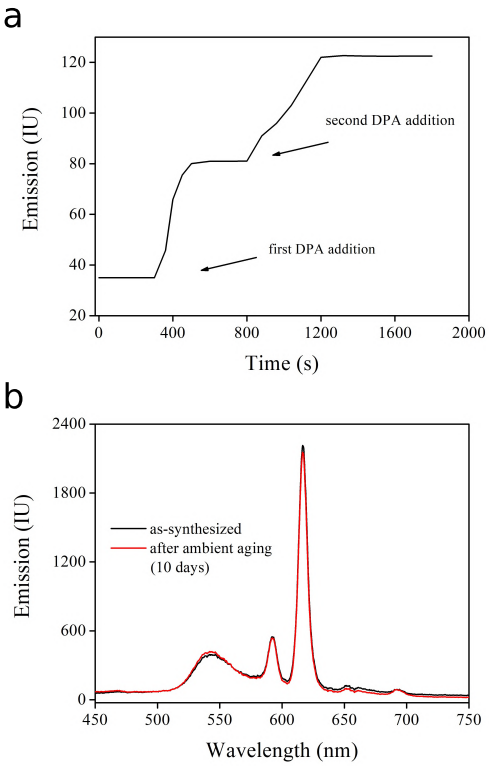

Fig. 4 Emission intensity monitoring of RPh@EuBTC at 552 nm (a) upon dropwise addition of DPA, and emission spectra (b) of as-synthesized RPh@EuBTC and RPh@EuBTC after ambient aging for 10 days; IU = intensity unit.

Response time and signal stability

In order to gain deeper insight into the sensing behavior of RPh@EuBTC towards DPA, the rose bengal emission intensity (552 nm) is monitored as DPA was gradually added to the RPh@EuBTC suspension. As depicted in Fig. 4, the rose bengal emission of RPh@EuBTC is weak in the absence of DPA. However, a noticeable increase in emission is observed

within just 10 s after the addition of DPA, indicating a rapid sensing response. This increasing trend in emission becomes gradual after 200 s, suggesting that RPh@EuBTC has completed its sensing response. For comparison, the response time is defined as the time taken by RPh@EuBTC to reach 50% of its maximum emission intensity after the addition of DPA [18, 19, 22]. In this instance, RPh@EuBTC exhibits a response time of 75 s. This value is comparable to the literature values [23–25]. The porous structure of the supporting lattice of EuBTC is likely responsible for efficiently adsorbing and transporting DPA molecules to the sensing molecules, thereby contributing to this rapid sensing response.

Another aspect requiring careful examination is the photostability of RPh@EuBTC, given that its fluorescent sensing relies on the quantification of emission intensity. To tentatively evaluate its photostability, the emission spectra of RPh@EuBTC are measured before and after aging for ten days under ambient conditions. As depicted in Fig. 4, no discernible difference is observed between these two emission spectra, either in emission wavelength or in intensity. This observation confirms a high level of photostability, ensuring the accuracy of fluorescent sensing with RPh@EuBTC.

Selectivity

In most practical sensing cases, the analyte is often dispersed within a complex environment filled with various competing species. Thus, achieving a distinct sensing response specific to the analyte, known as selectivity, is crucial for accurate readings. The selectivity of RPh@EuBTC is preliminarily assessed by examining its absorption and emission spectra in the presence of DPA and several representative interferents (100 μM), including benzoic acid (BA), p-hydroxybenzoic acid (HA), p-toluic acid (TA), o-phthalic acid (PA), D-aspartic acid (Asp), glycine (Gly), methionine (Met), and protons (pH = 4.0). As illustrated in Fig. 5, only the presence of DPA enhances the rose bengal absorption (528 nm) of RPh@EuBTC, while most interferents show no significant effects on enhancing RPh@EuBTC's rose bengal absorption, except for the protons that trigger the probe structural transformation. There is no evidence of spectral shifts, new absorption bands, or shoulder peaks, indicating minimal interactions between RPh@EuBTC's rose bengal probe and these interferents. This observation confirms the good selectivity of RPh@EuBTC for colorimetric sensing. Additionally, it is noted that the rose bengal absorption of RPh@EuBTC is marginally enhanced by HA, PA, and Gly. This is attributed to their ability to release protons, thereby inducing structural transformation of rose bengal. However, their interfering effects are minimal and acceptable when compared to literature reports [26, 27].

Meanwhile, the selectivity of RPh@EuBTC in ratiometric fluorescent sensing is discussed by comparing its emission spectra in the presence of DPA and the aforementioned interferents (100 μM). As shown in Fig. 5, only the presence of DPA enhances the rose bengal emission (552 nm) of RPh@EuBTC, while the interferents have no effects on enhancing RPh@EuBTC's rose bengal emission. Conversely, RPh@EuBTC's Eu emission intensity is reduced only in the presence of DPA and remains unaffected with all interferents. This finding is consistent with the case of RPh@EuBTC's rose bengal absorption. The interferents have minimal impacts on RPh@EuBTC's emission, whether on the rose bengal or Eu emission component, suggesting limited interactions between RPh@EuBTC and the interferents. To compare the selectivity of RPh@EuBTC, the emission intensity ratios of $F_{552\,nm}/F_{616\,nm}$ for these interferents are plotted. As depicted in the inset of Fig. 5, a high $F_{552\,nm}/F_{616\,nm}$ value (2.61) is observed only in the presence of DPA, while the interferents yield low $F_{552\,nm}/F_{616\,nm}$ values below 0.25. This confirms the robust selectivity of RPh@EuBTC's ratiometric fluorescent sensing.

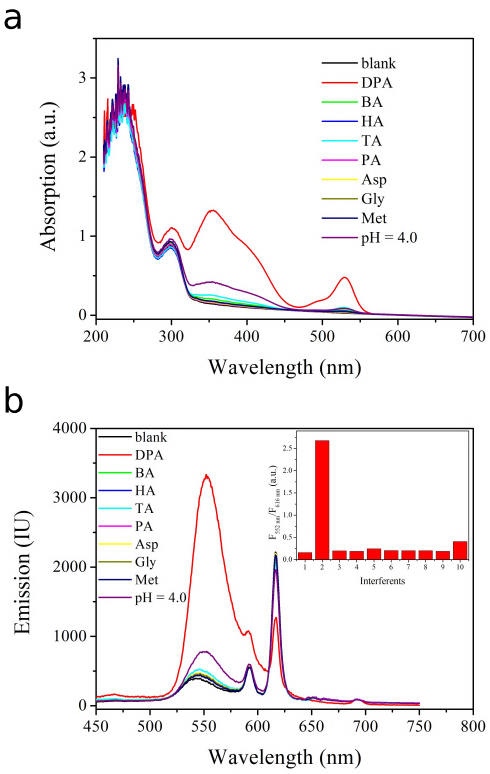

Fig. 5 Absorption (a) and emission (b) spectra of RPh@EuBTC suspension in ethanol (0.05 mg/ml) in the presence of representative interferents (100 μM); a.u. = absorbance unit, IU = intensity unit. Inset: corresponding $F_{552\,nm}/F_{616\,nm}$ ratios, where 1 = blank, 2 = DPA, 3 = BA, 4 = HA, 5 = TA, 6 = PA, 7 = Asp, 8 = Gly, 9 = Met, and 10 = protons (pH 4.0).

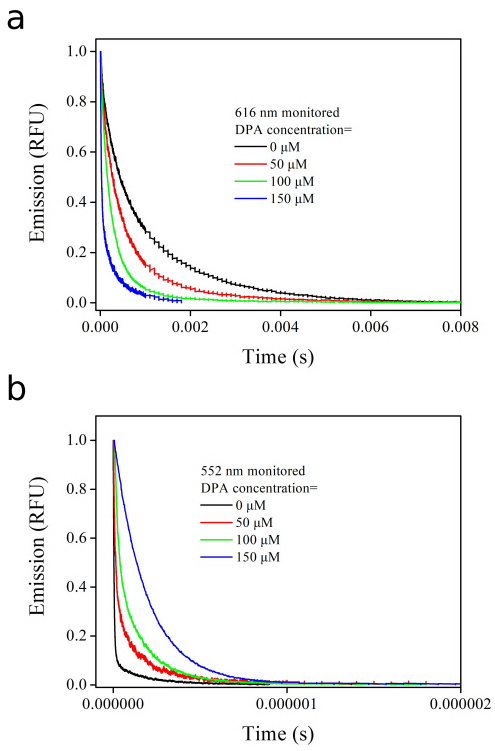

Fig. 6 Emission decay dynamics of RPh@EuBTC for the Eu emission component at 616 nm (a) and the rhodamine emission component at 552 nm (b) under various DPA concentrations; RFU = relative fluorescence unit.

Table 1 Emission decay lifetimes of RPh@EuBTC's two emission components under various DPA concentrations.

DPA concentration (μM)	0	50	100	150
Rhodamine emission (552 nm, ns)	7.0	74.3	101.6	189.1
Eu emission (616 nm, μs)	1000.3	554.3	280.6	140.3

Sensing mechanism

Based on the above discussion about RPh@EuBTC's sensing performance, a plausible sensing mechanism is proposed as follows. A DPA molecule consists of two parts: a pyridine ring and two hydroxyl groups. The pyridine ring, with its electron-withdrawing nature, likely captures excited state electrons from EuBTC, prompting an electron-transfer phenomenon and the subsequent quenching of RPh@EuBTC's Eu emission. Furthermore, the increased acidity of the two hydroxyl groups due to the pyridine's electron-withdrawing nature may lead to proton release. Consequently, a structural transformation favoring emission enhancement is observed in RPh@EuBTCs rose bengal part. In summary, DPA quenches RPh@EuBTC's Eu emission while amplifying its rose bengal emission. To substantiate this statement, the emission decay lifetimes of RPh@EuBTC's two emission components at various DPA concentrations are measured and tabulated in Table 1. As depicted in Fig. 6, both emission components (552 nm and 616 nm) exhibit a single exponential decay mode across different DPA concentrations. With increasing DPA concentrations, the lifetime of RPh@EuBTC's rose bengal emission component increases from 7.0 ns (DPA concentration = 0 μM) to 189.1 ns (DPA concentration = 150 μM), indicating that rhodamine molecules in RPh@EuBTC begin to take their emissive xanthene structure in the presence of DPA [18]. Conversely, the lifetime of RPh@EuBTC's Eu emission component decreases from 1000.3 μs (DPA concentration = 0 μM) to 140.3 μs (DPA concentration = 150 μM), due to the electron transfer from the Eu emissive center to DPA's pyridine ring [27]. To elaborate, the sensing mechanism of RPh@EuBTC towards DPA consists of rose bengal probe's emission turn-on effect and the Eu-based supporting lattice's emission turn-off effect. The former stems from the structural transformation of rose bengal induced by DPA-released protons, while the latter arises from the electron transfer from EuBTC to DPA.

Table 2 Ratiometric fluorescent sensing result of RPh@EuBTC.

DPA added (μM)	detected (μM)	error
0	1.3	N/A
50	47.5	95.0
100	103.3	103.3
150	142.1	94.7

Practical sensing performance of RPh@EuBTC towards DPA

To assess the practical sensing performance of RPh@EuBTC, its colorimetric and ratiometric fluorescent sensings are evaluated using real-world samples containing varying concentrations of DPA. As depicted in Fig. 2, RPh@EuBTC appears nearly transparent under natural light when DPA is absent. However, when the DPA concentration reaches 10 μM, the RPh@EuBTC suspension becomes a distinct pink hue, which is discernible to the naked eye. This observation validates the feasibility of colorimetric sensing with RPh@EuBTC, including the potential for visual detection. Additionally, with the fluorescent calibration curve established previously, the ratiometric fluorescent sensing performance of RPh@EuBTC is investigated. Due to the non-linearity of this curve, the precision is somewhat unsatisfactory, leading to noticeable sensing errors, as indicated in Table 2. Nonetheless, the preceding analysis underscores the distinctive advantage of RPh@EuBTC over conventional MOF sensing materials, attributed to its dual sensing modalities and the prospect of visual detection [26, 27].

CONCLUSION

In summary, this study presents an optical sensing platform for the biomarker DPA, using the rare earth luminescent MOF EuBTC as the supporting lattice and RPh as the sensing probe. The microstructure of RPh@EuBTC was validated through XRD, IR, TGA, and photophysical spectra analyses. Two distinct sensing behaviors were observed with RPh@EuBTC: colorimetric sensing based on absorption and ratiometric fluorescent sensing based on fluorescence. While the rose bengal emission exhibited an emission turn-on effect in the presence of DPA, showing an increase in fluorescence intensity, the Eu emission component experienced a turn-off effect, showing a decrease in emission intensity. The sensing response followed a linear trend with a LOD value of 2.2 μM. The sensing mechanism was the combination of the emission turn-on effect of the rose bengal probe and the emission turn-off effect of the Eu-based supporting lattice. This composite structure demonstrated superiority over traditional MOF sensing materials due to its dual sensing behaviors and possibility for visual detection. To enhance performance further, improvements in the linearity of ratiometric fluorescent sensing are desired.

Acknowledgements: This work was supported by our universities, and the authors thank the technique support from our universities, including the funds of Zhejiang Wanli University Introduces High-level Talent Research Startup Funding (SC1032410380140), 2024 Zhejiang Provincial Department of Education Research Project (SC1032510380300), and 2024 Provincial College Students' Innovation and Entrepreneurship Training Program Project (110354112400181).

REFERENCES

1. Carlos LD, Assunção M, Mourão PM (1998) Luminescence of non-hygroscopic polymer electrolytes modified by europium picrate complexes. *Electro acta* **43**, 1365–1369.
2. Szuszkiewicz W, Keller B, Guzik M (2002) Application of lanthanide (Eu, Nd) spectroscopy as a structural probe of diluted double phosphates. *J Alloys Compd* **341**, 297–306.
3. Chuai XH, Zhang HJ, Li FS (2000) Luminescence properties of $Eu(phen)_2Cl_3$ doped in sol-gel-derived SiO_2-PEG matrix. *Mater Lett* **46**, 244–247.
4. Welker T (1991) Recent developments on phosphors for fluorescent lamps and cathode-ray tubes. *J Lumin* **49**, 49–56.
5. Zhang MS, Yin W, Su Q (2002) Encapsulation and luminescence of the nanostructured supramolecular material $[Eu(Phen)_4](NO_3)_{3/}(CH_3)_3Si—MCM—4_1$. *Mater Lett* **57**, 940–945.
6. Ronda CR (1997) Recent achievements in research on phosphors for lamps and displays. *J Lumin* **72–74**, 49–54.
7. Michel J, Digonnet F (2001) Rare-earth-doped fiber lasers and amplifiers. *Marcel Dekker Inc* **2001**, 329–330.
8. Niyomdecha N, Noisumdaeng P, Boonarkart C, Auewarakul P (2024) Effect of azo dye treatment on the detection of human (OC43) coronavirus surrogate and SARS-CoV-2 viability based on an in-house photoactivator device. *ScienceAsia* **50**, ID 2024077.
9. Long W, Huang S, Huang Y (2023) Selective catalytic hydrogenation of furfural to cyclopentanone over Ru-Co bimetallic catalyst. *ScienceAsia* **49**, 116–123.
10. Cao LA, Wei M, Wu Z, Zhang Z, Wang D, Zhao T, Hu L (2025) Enhancing non-enzymatic glucose electrochemical sensing performance with ZnO@ZIF-67 nanoarrays. *ScienceAsia* **51**, ID 2025033.
11. Shu Q, Yang L, Zhang X, Yang F, Huang P (2025) Germanium quantum dots prepared by direct annealing of as-deposited amorphous films: Structure and optical properties. *ScienceAsia* **51**, ID 2025036.
12. Snitzer E (1961) Proposed fiber cavities for optical lasers. *J Appl Phys* **32**, 36–39.
13. Zhao YL, Zhao FY (2000) Synthesis and characterization of a series rare earth trinary complexes with cinnamic acidando-phenanthroline. *J Rare Earths* **18**, 318–321.
14. Hench LL, West JK (1990) The sol–gel process. *Chem Rev* **90**, 33–72.
15. Lan EH, Dunn B, Zink JI (2000) Sol–gel encapsulated anti-trinitrotoluene antibodies in immunoassays for TNT. *Chem Mater* **12**, 1874–1878.
16. Rouse JH, MacNeil BA, Ferguson GS (2000) Sol–gel processing of ordered multilayers to produce composite films of controlled thickness. *Chem Mater* **12**, 2502–2507.
17. Husing N, Schubert U (1998) Aerogels–airy materials: Chemistry structure and properties. *Angew Chem Int Ed* **37**, 22–45.
18. Bhatia RB, Brinker CJ (2000) Aqueous sol–gel process for protein encapsulation. *Chem Mater* **12**, 2434–2441.
19. Brinker CJ, Scherer GW (1990) *Sol–Gel Science, the Physics and Chemistry of Sol–Gel Processing*, Academic Press, San Diego, CA, pp 15–16.
20. Cerven G, Corriu RJ P, Framery E (2001) Sol–gel process–influence of ageing on the textural properties of organosilsesquioxane materials. *J Mater Chem* **11**, 713–717.
21. Sun L, Zhang H, Peng C, Yu J, Meng Q, Fu L, Liu F, Guo X (2006) Covalent linking of near-infrared luminescent ternary lanthanide (Er^{3+}, Nd^{3+}, Yb^{3+}) complexes on functionalized mesoporous MCM-41 and SBA-15. *J Phys Chem B* **110**, 7249–7258.
22. Sun L, Yu J, Zhang H, Meng Q, Ma E, Peng C, Yang K (2007) Near-infrared luminescent mesoporous materials covalently bonded with ternary lanthanide [Er(III), Nd(III), Yb(III), Sm(III), Pr(III)] complexes. *Microporous Mesoporous Mater* **98**, 156–165.
23. Peng C, Zhang H, Yu J, Meng Q, Fu L, Li H, Sun L, Guo X (2005) Synthesis, characterization, and luminescence properties of the ternary europium complex covalently bonded to mesoporous SBA-15. *J Phys Chem B* **109**, 15278–15287.
24. Sprintchnik G, Sprimtchnik HW, Kirsch PP (1977) Preparation and photochemical reactivity of surfactant ruthenium(II) complexes in monolayer assemblies and at water-solid interfaces. *J Am Chem Soc* **99**, 4947–4954.
25. Malins C, Fanni S, Glever HG (1999) The preparation of a sol–gel glass oxygen sensor incorporating a covalently

bonded fluorescent dye. *Anal Commun* **36**, 3–4.
26. Ding JJ, Li B, Zhang HR, Lei BF, Li WL (2007) Oxygen-sensing properties of ormosil hybrid matrials doped with ruthenium(II) complexes via a sol–gel process. *Mater Lett* **61**, 3374.
27. Murtagh MT, Shahriari MR, Krihak M (1998) A study of the effects of organic modification and processing technique on the luminescence quenching behavior of sol–gel oxygen sensors based on a Ru(II) complex. *Chem Mater* **10**, 3862–3869.